Pergamon

Int. J. Solids Structures Vol. 32, No. 17/18, pp. 2609–2626, 1995

0020-7683/95 $9.50 + .00

0020-7683(94)00285-1

DYNAMIC FAILURE MECHANISMS IN A 6061-T6 Al/Al_2O_3 METAL–MATRIX COMPOSITE

D. R. CHICHILI and K. T. RAMESH
Department of Mechanical Engineering, The Johns Hopkins University, Baltimore, MD 21218, U.S.A.

(*Received* 3 *February* 1994)

Abstract—The dynamic failure of an alumina particle-reinforced 6061-T6 aluminum alloy composite has been studied using a tension Kolsky bar, and the process of fracture has been investigated using scanning electron microscopy. The failure of a 6061-T6 aluminum alloy was also studied for purposes of comparison. The composite was found to fail in a macroscopically brittle manner in tension, with a failure strain that increased with the nominal strain rate. Differences in hardening rate that are observed in dynamic tension and compression are ascribed to the development of internal damage within the composite in the form of particle cracking. Examination of the fracture surface of the monolithic alloy after dynamic failure shows a ductile failure through void nucleation, growth and coalescence, with substantial void sheet formation. Examination of the fracture surface of the composite after dynamic failure shows microscopically ductile failure in the matrix following brittle cracking of the particles. The dynamic failure process is hypothesized to consist of: (a) cracking of the reinforcing particles; (b) partial debonding at the particle–matrix interface resulting in the nucleation of voids within the matrix; and (c) the growth and coalescence of voids in the matrix to form the final failure surface. The failure process itself quickly localizes within the specimen, so that only a small part of the specimen is affected by all of the damage processes of particle cracking, interface failure and void growth.

1. INTRODUCTION AND BACKGROUND

The increasing utilization of particle-reinforced metal–matrix composites (MMCs) within structural applications has been driven by the high specific stiffness and specific strength exhibited by these materials, combined with a relative ease of manufacture. The primary factor inhibiting even more widespread application of particle-reinforced MMCs is their relatively low ductility (compared with that of the matrix metal). Thus a significant scientific effort has been devoted to the determination of the micromechanisms through which fracture occurs within these composites under quasistatic loadings. This paper describes an investigation of the *dynamic* failure of a particle-reinforced MMC, with the intent of determining the micromechanisms that are active during the *dynamic* failure process.

When the failure process is viewed as the result of the evolution of (several) damage mechanisms, it is clear that the development of failure is also intimately related to the microscopic processes associated with macroscopically homogeneous deformations. Thus any study of failure in MMCs must be rooted in an understanding of the material behavior under macroscopically homogeneous deformations. Fortunately such an understanding (in a broad sense) has largely been developed for quasistatic deformations [e.g. Arsenault and Wu (1987); Christman *et al.* (1989b); Evans *et al.* (1991); Lewandowski *et al.* (1989); Liu *et al.* (1989); Nair *et al.* (1985); Yang *et al.* (1991)]. The stress–strain response, and the effect of material parameters such as reinforcement size [e.g. Lewandowski *et al.* (1991)], volume fraction [e.g. Evans *et al.* (1991)], aspect ratio [e.g. Yang *et al.* (1991)] and distribution [e.g. Lewandowski *et al.* (1989)] on the stress–strain response have been studied extensively for the quasistatic case. The dynamic behavior of particle-reinforced MMCs has been studied by Espinosa and Clifton (1991), Harding *et al.* (1987), Marchand *et al.* (1988) and more recently over a very wide range of strain rates by Yadav *et al.* (1995).

The ductility of a ceramic particle reinforced MMC is typically less than a fifth that of the matrix metal alone. Studies of the loss of ductility of MMCs have therefore focused on understanding the microscopic failure mechanisms that result from the presence of a hard, brittle reinforcement phase in a relatively soft, ductile matrix [e.g. Christman *et al.* (1989b);

Davidson (1991); Kamat *et al.* (1989); Lewandowski *et al.* (1989); Llorca *et al.* (1991); Lloyd (1991); Papazian and Adler (1990); Zhou *et al.* (1991)]. To a first approximation, there are three major damage modes that may be active in such materials: fracture of the reinforcement phase, failure of the particle–matrix interface, and failure of the matrix phase itself. The dominant damage mode is determined by microstructural features such as particle size [e.g. Flom and Arsenault (1989)] and distribution, particle volume fraction, the interface characteristics, as well as prior thermomechanical processing [Brechet *et al.* (1991); Hunt *et al.* (1991); Lewandowski *et al.* (1989); Mummery and Derby (1991); Yang *et al.* (1990)].

The effects of heat treatment and of reinforcement size on the tensile fracture of SiC_p-reinforced aluminum alloy were studied by Singh and Lewandowski (1993). They found that the dominant mode of microfailure changes from particle fracture in an underaged material to failure near the particle–matrix interface and failure in the matrix for an overaged condition. Liu and Lewandowski (1993) studied the effects of superimposed hydrostatic pressure on the deformation and fracture of an Al_2O_3 particle-reinforced 6061 Al composite, and observed that the ductility of the composite increased with hydrostatic pressure. Christman *et al.* (1989b) observed that the presence of SiC whiskers in 2124 aluminum leads to a significant build-up of hydrostatic stresses in the matrix during plastic deformation, and concluded that void formation in the matrix as well as at the whisker–matrix interface played an important role. Several models have been developed to examine the initiation and development of damage in such composites subjected to quasistatic loading [e.g. Bao (1992); Clegg (1988); Tvergaard (1990)].

In contrast to the quasistatic case, the mechanisms that are active during the dynamic failure of particle-reinforced MMCs are not well understood. Marchand *et al.* (1988) and Cho *et al.* (1991) examined the dynamic fracture of a SiC whisker-reinforced 2124 aluminum alloy and observed that the dynamic fracture toughness was substantially higher than the quasistatic fracture toughness but decreased as the volume fraction of whiskers increased. Void nucleation was found to occur at the ends of the SiC whiskers; some whisker pullout was also observed. Perng *et al.* (1993) examined the tensile behavior of an Al_2O_3 particle-reinforced 6061 aluminum composite at low temperatures and observed very little dependence of the total elongation on the strain rate. However, Harding *et al.* (1987) found that the failure strain of an SiC whisker-reinforced aluminum composite increased with increasing strain rate.

It is the intent of this paper to develop an understanding of the dynamic failure of an alumina-reinforced aluminum composite, based on a clear understanding of the homogeneous deformations of the composite and the matrix material under dynamic conditions, and drawing on microscopic observations of the failure mode.

2. MATERIALS

The materials under investigation are a 6061 aluminum alloy reinforced with alumina particles (commercially available from Duralcan Corp.) and unreinforced 6061-T6 aluminum alloy as a comparison material. Table 1 provides the chemical composition of the matrix of the composite. The reinforcement phase in the composite consists of calcined alumina (Al_2O_3) particles, with the chemical composition given in Table 2. The volume

Table 1. Chemical composition of the matrix of the composite (manufacturer's data)

Si	Fe	Cu	Mn	Mg	Cr	Zn	Ti
0.72	0.09	0.27	0.004	0.90	0.10	0.01	0.008

Table 2. Chemical composition of the alumina particles (manufacturer's data)

Al_2O_3	Na_2O	SiO_2	Fe_2O_3
99.0 min.	0.40 max.	0.04 max.	0.04 max.

Table 3. Comparison of the mechanical properties of the composite and of the monolithic 6061-T6 aluminum alloy (manufacturer's data)

Material	Young's modulus (GPa)	Yield strength (MPa)	Tensile strength (MPa)	Elongation at failure (%)
6061-T6 Al	69	276	311	20
Al/Al_2O_3 Composite	97	352	372	3–4

fraction of the particles in the composite is 20%. The mean particle size is 21 ± 2 μm, with 94% of the particles smaller than 33 μm and 3% smaller than 10 μm; the particles are plate-like, with aspect ratios ranging from 3 : 1 to 8 : 1.

The composite was made by mixing alumina particles with the molten metal, followed by die casting and hot extrusion. The composite was then given a T-651 heat treatment designed by the manufacturer. This involved solution treatment for 2 h at 560°C followed by quenching in water, and then aging for 10 h at a temperature of 177°C. Figure 1 shows typical scanning electron micrographs of the extruded Al/Al_2O_3 composite along and transverse to the extrusion axis. The micrographs show a relatively uniform distribution of the particles with a perceptible preferred orientation along the extrusion axis. The composite has an overall porosity of less than 0.8% by volume. Table 3 lists nominal values for the mechanical properties of the composite, as provided by the manufacturer, together with (for comparison) the properties of the monolithic 6061-T6 alloy.

The matrix of the composite and the monolithic alloy were compared in terms of Knoop microhardness and in terms of Mg_2Si precipitate size. The load for the microhardness measurement was chosen so that the length of the long diagonal of the indentation in the matrix was less than half the distance to the nearest particles. The measurements showed that there was no appreciable difference between the microhardness of the matrix and that of the monolithic alloy. Mg_2Si precipitate sizes in the matrix of the composite and in the monolithic alloy were measured using scanning electron microscopy. The average precipitate sizes in both the matrix and in the monolithic alloy were found to be 2 μm. Note that Strangwood *et al.* (1991) studied interfacial segregation in Al-based MMCs and found that the Al_2O_3/Al interface was Mg rich. This solute segregation suggests that the volume fraction of the Mg_2Si precipitate in the matrix of the composite should be less than that in the monolithic alloy.

3. DYNAMIC BEHAVIOR OF MATERIALS: HOMOGENEOUS DEFORMATIONS

We summarize here the results of Yadav *et al.* (1995) on the dynamic behavior of the identical Al_2O_3/6061-T6 aluminum composite during homogeneous deformations in compression and shear at strain rates of 10^{-4}–10^{6} s^{-1}. A combination of compression Kolsky bar (Ramesh and Coates, 1992), torsional Kolsky bar (Ramesh, 1994) and high strain rate pressure shear plate impact techniques (Clifton and Klopp, 1985) were used to obtain the required strain rates. The reader is referred to Yadav *et al.* (1995) for a more complete description of the experiments and for other relevant results.

Figure 2 shows a comparison of the dynamic stress–strain curves (in compression) at 3.5×10^{3} s^{-1} for both the monolithic alloy and the composite; it is clear that the composite displays increased strength (due to the reinforcement) but essentially the same strain hardening behavior as the monolithic alloy (i.e. the matrix). Note that no damage is developed within the composite during these compressive deformations. One may estimate the rate-sensitivity of a material by plotting the stresses sustained (at a fixed strain) as a function of strain rate, using data (such as those in Fig. 2) over a wide range of strain rates. Such a rate-sensitivity diagram is presented for the composite and the 6061-T6 aluminum alloy in Fig. 3. Note that the composite is highly rate sensitive, especially at high strain rates (this response represents the effective behavior for this heterogeneous material). In

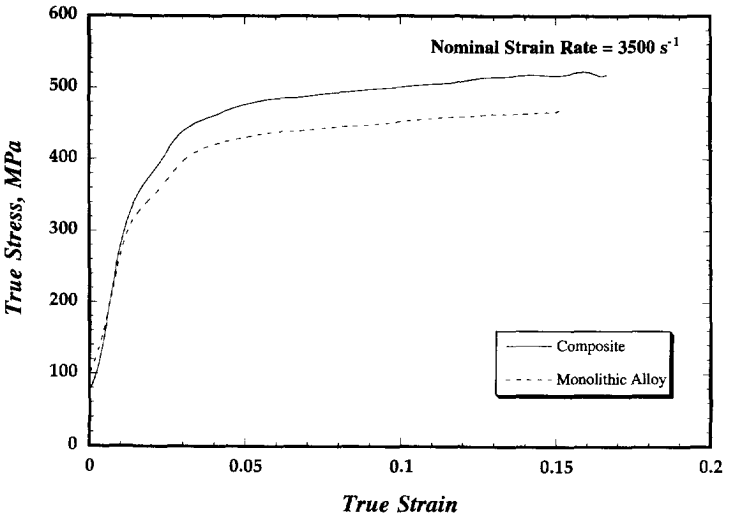

Fig. 2. True stress–strain curves for the composite and the monolithic alloy under a compressive strain rate of 3500 s^{-1}. The composite displays higher strength than the monolithic alloy but essentially the same strain hardening behavior.

particular, the composite displays a higher rate sensitivity than the monolithic alloy that constitutes the metal matrix [some possible explanations for this observed behavior are discussed by Yadav *et al.* (1995)]. It is important to note also that the monolithic alloy has substantial rate sensitivity at strain rates above $\sim 10^3$ s^{-1}. This is in disagreement with the general assumption that 6061-T6 is a rate-insensitive aluminum alloy [e.g. Rajendran *et al.* (1986)]; since the local strain rates during the dynamic fracture phenomenon are very high, this rate dependence may be expected to result in a higher fracture toughness under dynamic loading.

4. FAILURE MECHANISMS UNDER HIGH RATE TENSILE DEFORMATIONS

4.1. *Experimental technique: the tension Kolsky bar*

The standard torsional Kolsky bar technique has been adapted to develop tensile deformations at high strain rates. The device (Fig. 4) consists of two long metal bars that

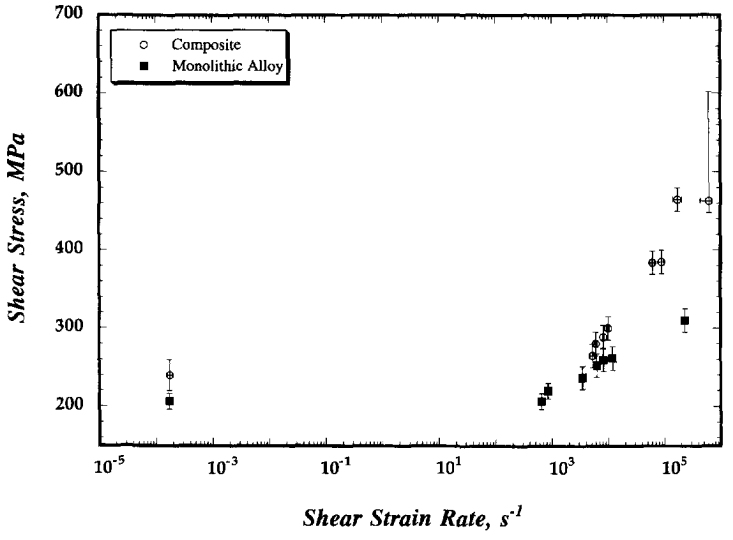

Fig. 3. Rate-sensitivity of the composite and of the monolithic (6061-T6 Al) alloy. The composite displays higher rate-sensitivity than the monolithic alloy.

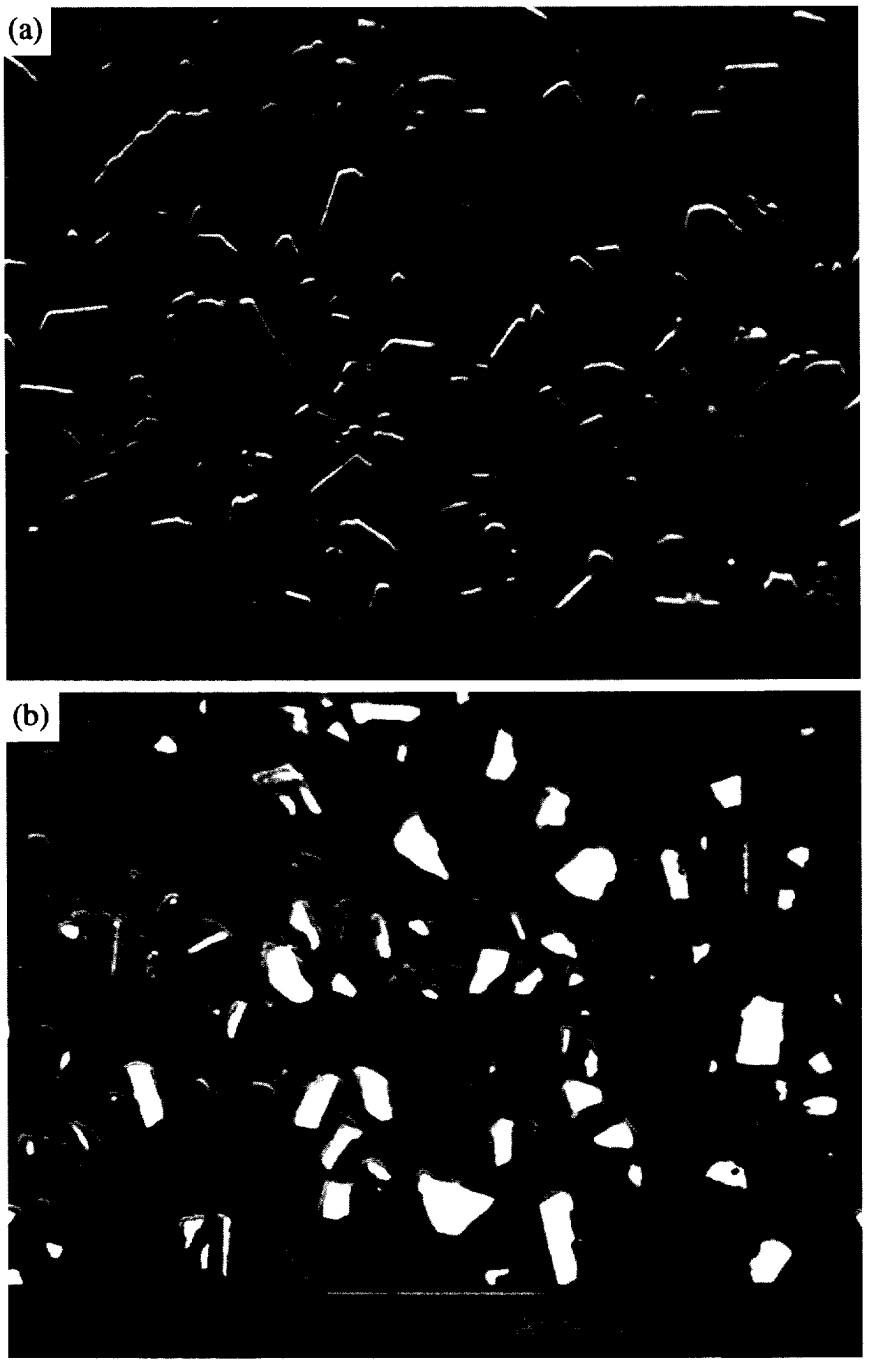

Fig. 1. Typical scanning electron micrograph of the extruded Al/Al_2O_3 composite (a) along the transverse axis and (b) along the extrusion axis, which is in the vertical direction. Some alignment of particles along the extrusion axis can be observed.

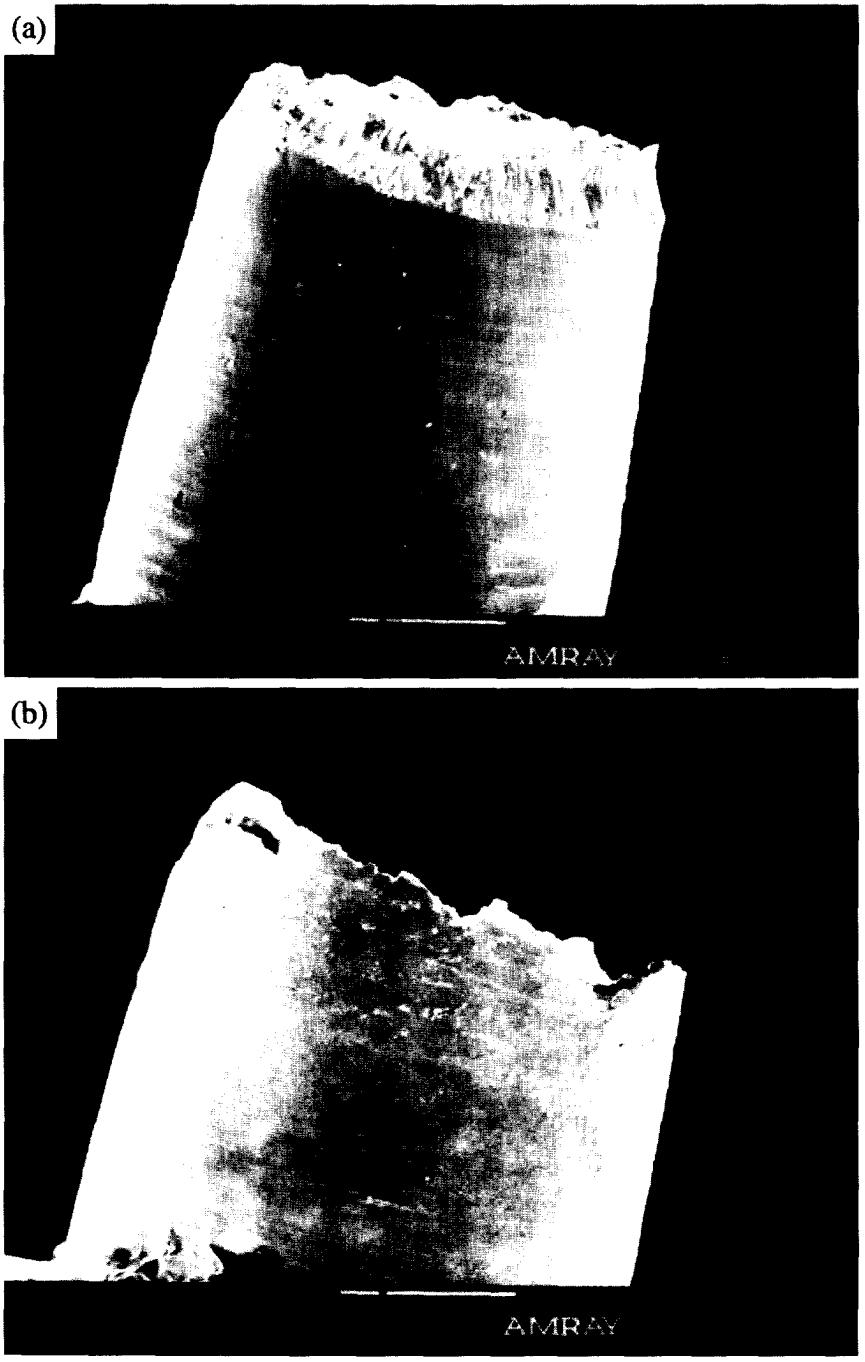

Fig. 10. (a) The macroscopic fracture surface (viewed edge on) of the monolithic alloy from a dynamic tension test, indicating the ductile fracture with large necking. (b) The macroscopic fracture surface (viewed edge on) of the composite developed during a dynamic tension test. One notes the macroscopically brittle fracture with little necking.

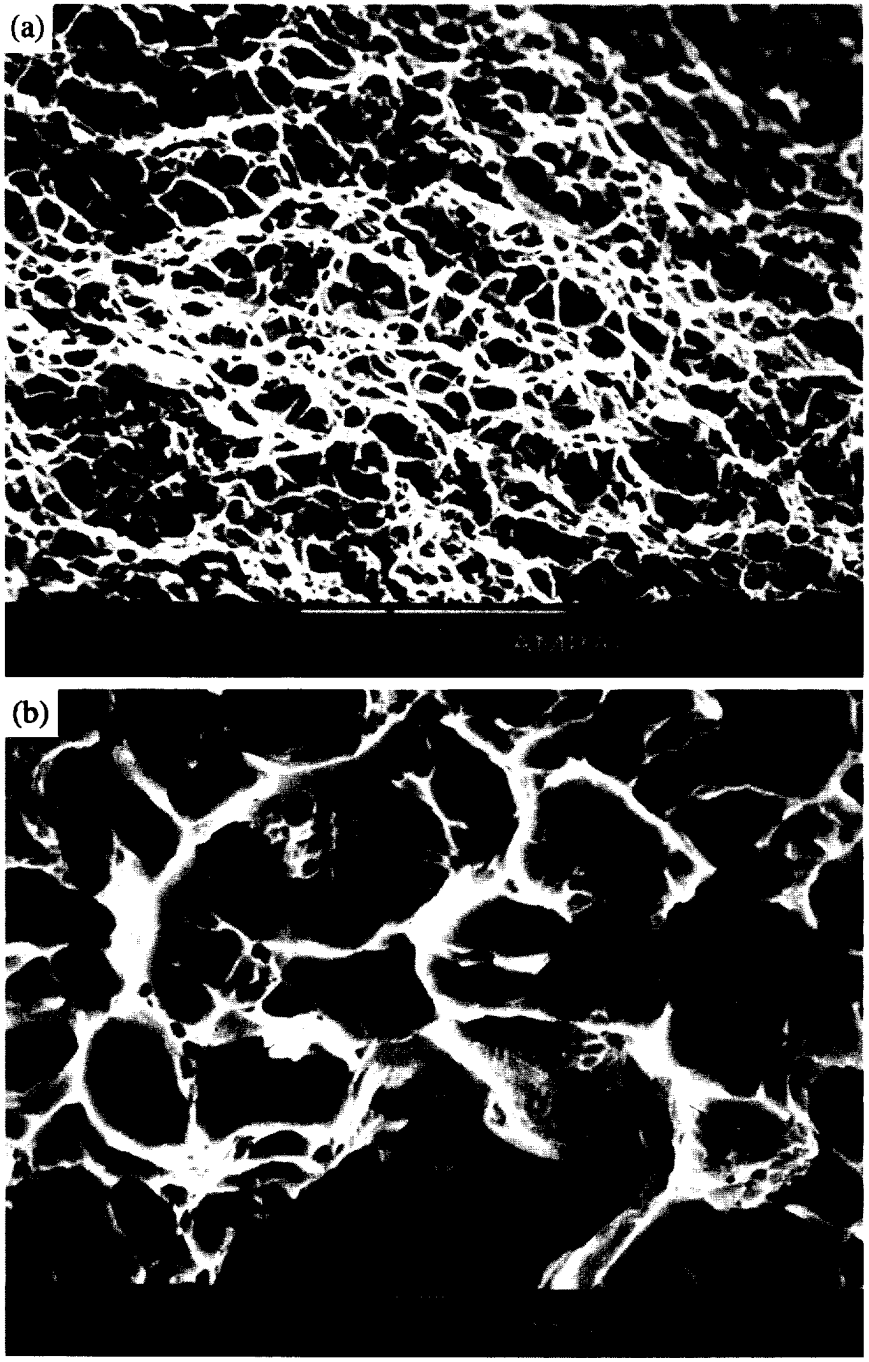

Fig. 11. (a) Micrograph of the fracture surface of the monolithic alloy indicating large dimples. (b) At higher magnification showing the smaller dimples resulting from void sheet formation.

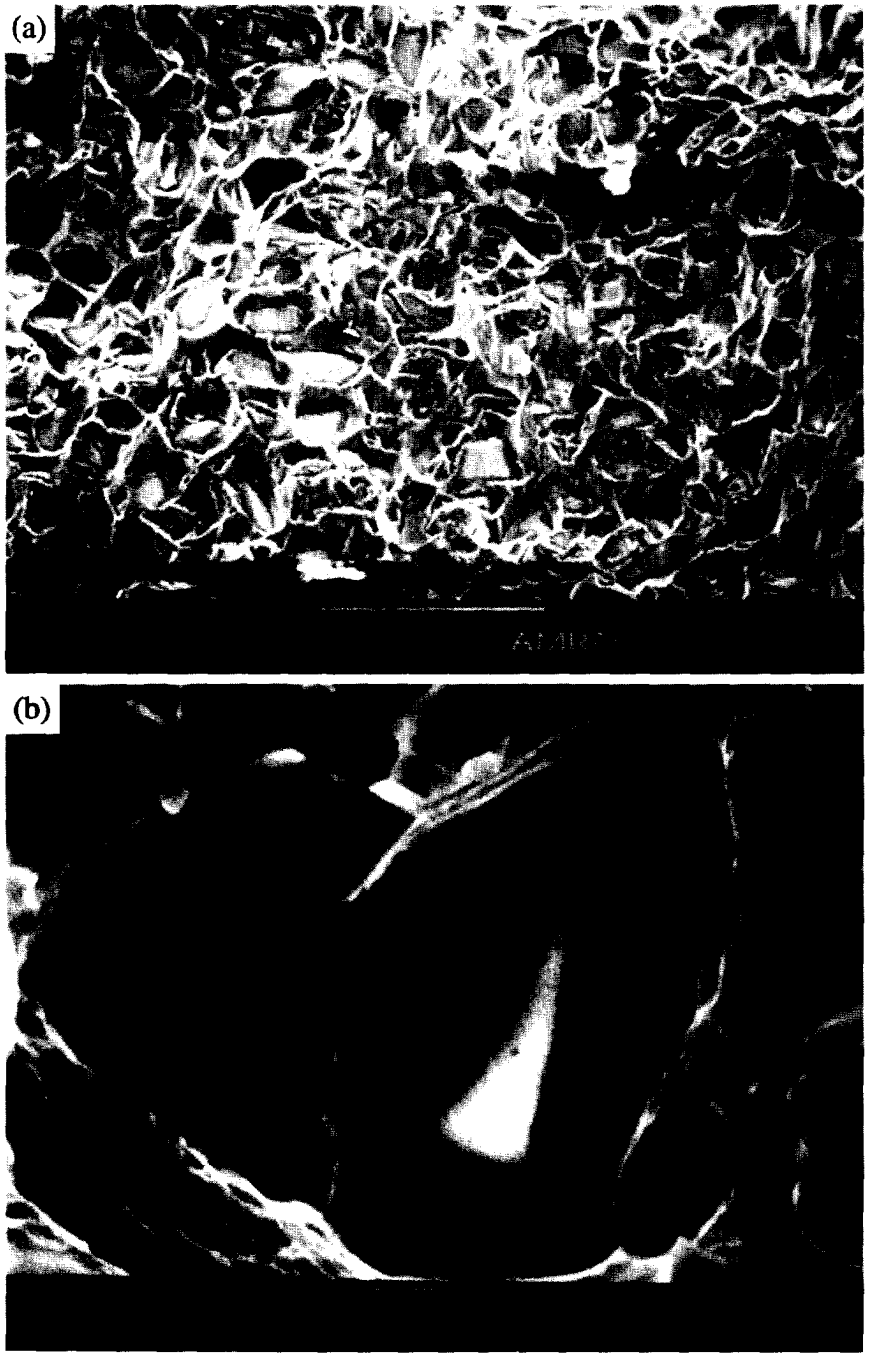

Fig. 12. (a) Micrograph of the fracture surface of the composite; most of the dimples contain fractured particles. (b) A higher magnification picture, showing interface debonding and an example of particle pullout.

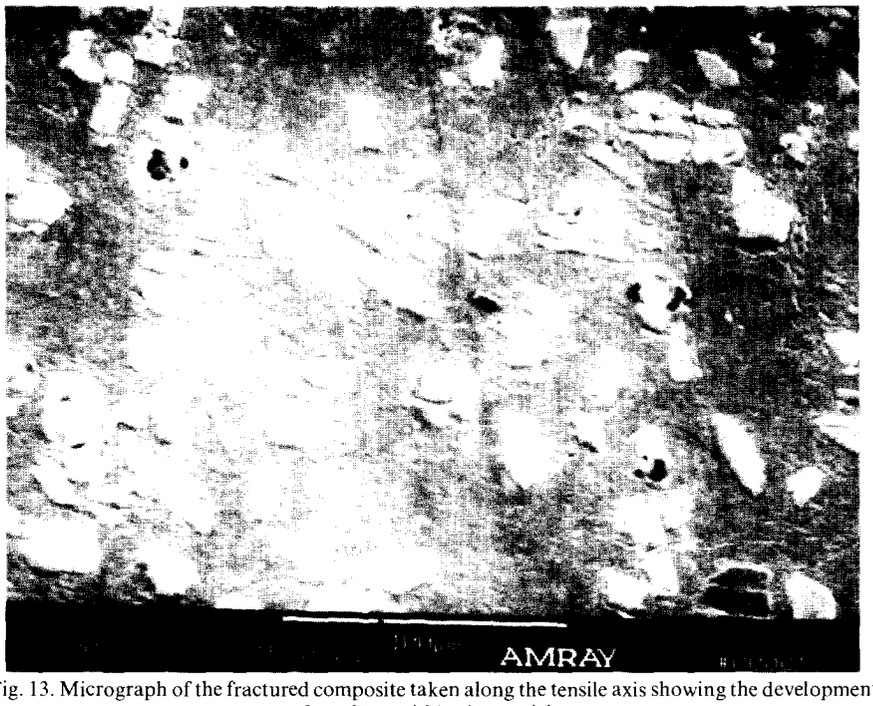

Fig. 13. Micrograph of the fractured composite taken along the tensile axis showing the development of cracking within the particles.

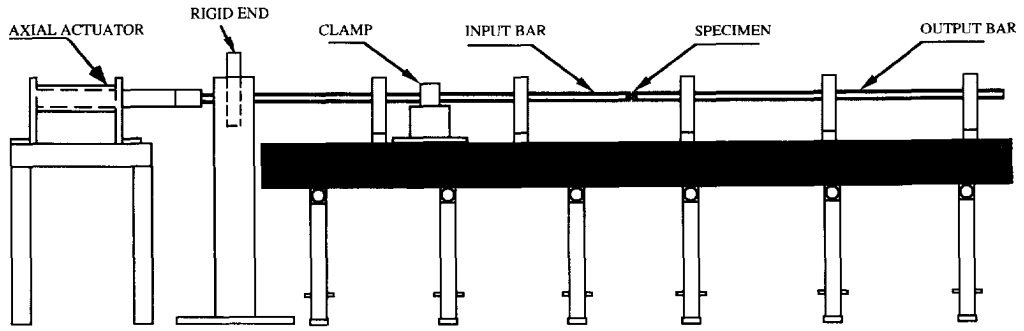

Fig. 4. Schematic diagram of the tension Kolsky bar.

are designed to remain elastic throughout the test. Strain gages are mounted on both the bars for measuring strain. A short cylindrical specimen (Fig. 5) is attached between the two bars using epoxy to attach the flanges to the ends of the bars. In operation, a tensile force is applied to a short section of the input bar using the hydraulic system; the rest of the input bar is restrained from extension using a friction clamp. When the friction clamp is suddenly released by breaking a pre-notched bolt, a tensile loading wave propagates down the bar while a compressive unloading wave propagates back into the pre-loaded section, dropping the tensile stress there to half its initial value. The unloading wave reflects from the end of the input bar (which acts as a rigid end condition) and drops the stress back to zero, thereby generating a tensile pulse. The pulse amplitude is half the stored tensile stress, and the pulse duration is determined by the length of the bar between the loading device and the clamp. The design of the friction clamp is critical; if the mechanism of release is asymmetrical, flexural waves will also be generated in the bar. Bar alignment and the clamping arrangement are adjusted until the bending waves (measured in the bar using a separate set of strain gages) are negligible.

The tension pulse propagates down the bar at the longitudinal wave velocity, arrives at the specimen, and is partly transmitted and partly reflected. After several reverberations of the wave within the specimen, the tensile stress in the specimen becomes nominally uniform. Once this state has been achieved, the transmitted pulse gives the stress history of the specimen directly, while the reflected pulse provides the strain rate history within the specimen. Proceeding along lines analogous to those for the compression Kolsky bar, the mean flow stress $\bar{\sigma}_s$ within the specimen and the nominal specimen strain rate $\dot{\bar{\varepsilon}}_s$ may be obtained from the relations

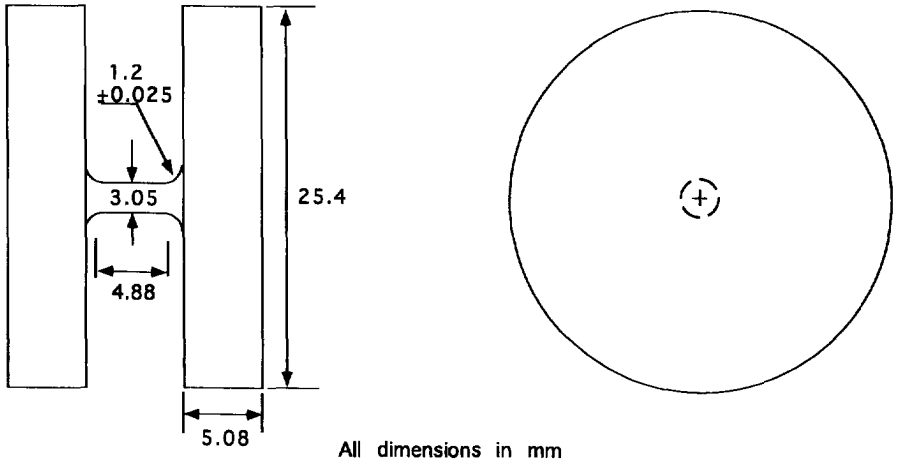

Fig. 5. The specimen used for the dynamic tension tests.

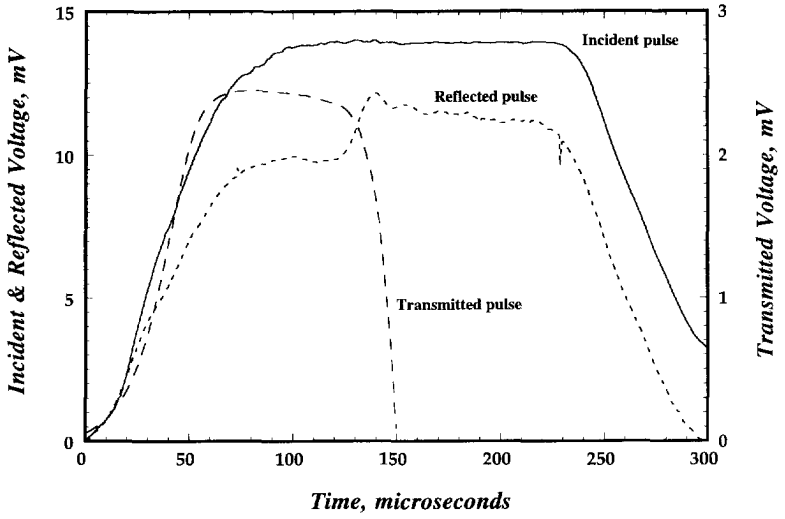

Fig. 6. Typical incident, reflected and transmitted pulses in the tension Kolsky bar.

$$\bar{\sigma}_s = \frac{EA_b}{A_s}\varepsilon_T$$

and

$$\dot{\bar{\varepsilon}}_s = \frac{2c_0}{l_s}\varepsilon_R,$$

where E is the Young's modulus of the bars, A_s and l_s are the specimen area and length, A_b and c_0 represent the bar cross-section area and the bar velocity, and ε_R and ε_T represent the strains in the input and the output bars, respectively. The strain rate history can then be integrated over time to get the specimen strain. Hence such a Kolsky bar test provides a complete stress–strain curve for a specimen homogeneously deformed under tension at a high strain rate.

Staab & Gilat (1991) performed a parametric study on the dimensions of the specimen for high strain rate tension testing using the split Hopkinson bar. They found that the results are independent of the dimensions of the specimen for specimen length-to-diameter ratios greater than 1.6, and that a one-dimensional stress–strain analysis could be used for analyzing the data. Hence for the present investigation the specimen length-to-diameter ratio is taken to be 1.6. A small fillet radius is provided to minimize the stress concentrations near the flanges.

Typical examples of the incident, reflected and transmitted pulses are shown in Fig. 6. The risetimes obtained in this Kolsky bar are of the order of 70 μs, while the pulse durations for the present investigation vary from 250 to 500 μs. The reflected pulse shown is obtained for a test on the composite, and represents an effective strain rate of 750 s^{-1} (note that the strain rate is essentially constant during the deformation). The rise in the reflected pulse at 140 μs corresponds to the failure of the specimen. Failure of the specimen causes the transmitted stress to collapse before the tension unloading wave arrives from the loading mechanism. The reflected pulse is corrected for the drift in baseline that results from the small deviation of the end condition of the input bar from the ideal rigid condition. The corrections are based on a separate series of calibration experiments performed to evaluate the end condition alone.

The tension Kolsky bar used for the experiments described here uses input and output bars made of 7075-T6 aluminum; each bar is approximately 2 m long. The tension is applied using a hydraulic device, while the friction clamp uses a notched 2024-T6 aluminum bolt that is extended until fracture by means of another hydraulic system. The strain gage signals are captured on a Nicolet 4049C digital oscilloscope. The strain rates obtained in tension using this system run as high as 1×10^3 s^{-1} for room temperature tests.

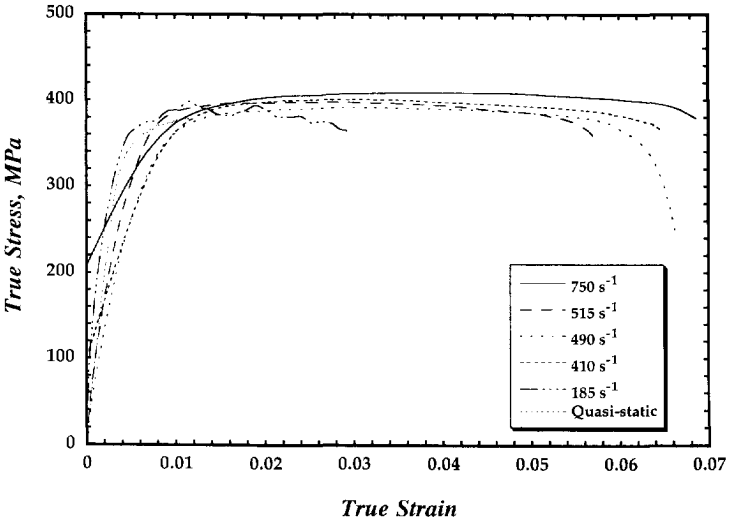

Fig. 7. Dynamic and quasistatic true stress true strain curves for the composite under tension. All the composite specimens failed during the initial loading pulse.

5. RESULTS AND DISCUSSION

The results of several dynamic tension tests on the alumina-reinforced aluminum composite (covering the range of strain rates from 10^2 to $8 \times 10^2\ s^{-1}$) are presented in Fig. 7. A stress–strain curve for the composite in quasistatic tension (data from the manufacturer) is also presented in Fig. 7. It is immediately apparent that the composite shows little or no strain hardening in tension, although the effective behavior of the composite showed the same strain hardening behavior as did the matrix in dynamic compression [Fig. 2, and Yadav *et al.* (1995)]. Such asymmetries in the behavior in tension and compression are often observed in MMCs, and are usually related to either residual stresses in the material [as a result of coefficient of thermal expansion (CTE) mismatch, for example] or to the development of internal damage in the form of particle cracking, interface debonding, or void growth.

We consider first the possibility that the observed tension–compression asymmetry is due to residual stresses arising from the mismatch in the CTE coupled with the thermomechanical processing involved in the production of the composite. Taggart and Bassani (1991) have examined the influence of residual stresses on the elastic–plastic behavior of particle-reinforced composites, assuming that the particles could be modeled as spherical inclusions. Neglecting debonding effects, they concluded that the overall response would be stiffer in tension than in compression. Arsenault and Taya (1987) examined the problem assuming ellipsoidal inclusions, and concluded that the yield stress in compression should be greater than that in tension for whisker-reinforced and fiber-reinforced composites, although they observed very little effect on the work-hardening rate. The latter model would predict no effect on the yield stress at all for spherical particles. The material examined in the present paper contains platelets rather than spheres or whiskers; however, the behavior of the composite in compression can be approximated very well (Yadav *et al.*, 1995) by assuming the particles are spherical using the unit cell model of Bao *et al.* (1991). The spherical approximation is probably a bad one in tension, since damage mechanisms are likely to develop; however, current models for the influence of the residual stress alone are unable to explain the observed dramatic decline in the strain hardening in tension as compared with compression.

Thus the tension–compression asymmetry is probably related to the development of internal damage within the material in the tension tests, resulting in a reduction in the effective strain hardening that is observed. Such effects have been observed in several other systems; e.g. Hunt *et al.* (1991) observed a decrease in work hardening in a model Al–Si–Mg composite with increasing particle size and volume fraction, and hypothesized that this

was a result of damage accumulation through particle cracking. Yang *et al.* (1990) examined the influence of particle cracking on the flow strength and the work hardening, viewing the microcrack damage as contributing additional plastic strain to the matrix and resulting in an effective softening. Brechet *et al.* (1991) examined the initiation of damage in MMCs in terms of particle cracking, looking in particular at particle size and aspect ratio, and also concluded that damage resulting from microcracking is likely to be a major mechanism when the size of the reinforcing particles is large (depending on the Weibull modulus of the particles). A micromechanical model using the unit cell approach has been developed by Bao (1992) for the case of the non-hardening matrix but accounting for particle cracking; again, the softening of the overall behavior as a result of the damage is predicted. All of these works indicate that particle cracking can be a major contributor to the difference in work hardening between compression and tension, and a significant degree of particle cracking is observed in our specimens (discussed subsequently). Since the composite shows strain hardening in compression, we hypothesize that significant damage due to particle cracking begins within the composite immediately after overall yield in tension, resulting in the negligible hardening observed. Several workers [e.g. Christman *et al.* (1989a); Lewandowski *et al.* (1989); Llorca *et al.* (1991)] have also shown that both the nucleation and growth of voids can contribute softening to the stress–strain curves of these composites and may be fundamentally important to the overall failure process. However, in the composite that we have studied here, our microscopic observations (described in the following) suggest that particle cracking represents the initial damage mode.

It may be noted from Fig. 7 that there is only a small increase in the flow stress with increasing strain rate (ignoring the initial parts of the dynamic stress–strain curves, when the stress state in the specimen is still non-uniform). This weak effect of the strain rate is largely consistent with the rate-sensitivity shown in Fig. 3, since the average strain rate is several hundred reciprocal seconds and the range of strain rates is not very large. Of course, it is conceivable that the occurrence of damage in these tensile tests also influences the apparent rate-sensitivity.

A result of particular interest that may be inferred from Fig. 7 is that the strain to failure increases with strain rate, on average. We note that all of the composite specimens fractured during the initial loading pulse, and that the specimens were all initially smooth without stress concentrators along the gage length. Thus the strain to failure is a meaningful quantity, representing the total strain that was developed before the cumulative nature of the damage caused overall failure. A plot of the strain to failure as a function of the strain rate is presented in Fig. 8 (the error bars shown for the failure strain correspond to the subjectivity associated with the choice of initial time in the integration of the strain rate history). Such an increase in the strain to failure with strain rate has also been observed by Harding *et al.* (1987) for an SiC_w-reinforced aluminum–matrix composite. Since Fig. 8 essentially shows an increase in the effective work required to cause failure with increasing strain rate, one may expect also that this material will have a dynamic fracture toughness that is greater than the quasistatic fracture toughness [some dynamic fracture tests, as in Cho *et al.* (1991), are planned as a follow up to this work]. The increase in strain to failure with increasing strain rate is hypothesized to result from the rate-sensitivity of the matrix material (Fig. 3), since the local rates during void growth and coalescence may be very high indeed, and it will be shown later that void growth represents one of the primary mechanisms during the latter stages of the failure process in this material.

For comparative purposes, Fig. 9 presents the quasistatic and dynamic behavior of the monolithic 6061-T6 alloy in tension. The monolithic alloy has a much greater ductility, as expected, and shows very little rate-sensitivity over this range of strain rates (it is important to remember that these tension Kolsky bar tests are unable to provide accurate constitutive information during the initial portions of the test—hence the inability to track the elastic modulus and the initial yield). The results in Fig. 9 are consistent with those of Staab and Gilat (1991). One should, of course, expect much higher strain rates within the failure zone in the composite, and the matrix material is rate-sensitive at higher strain rates (Fig. 3). Note the substantial strain hardening that is evinced by the monolithic alloy in dynamic tension. Thus, unlike the case of dynamic compression (Fig. 2), the monolithic

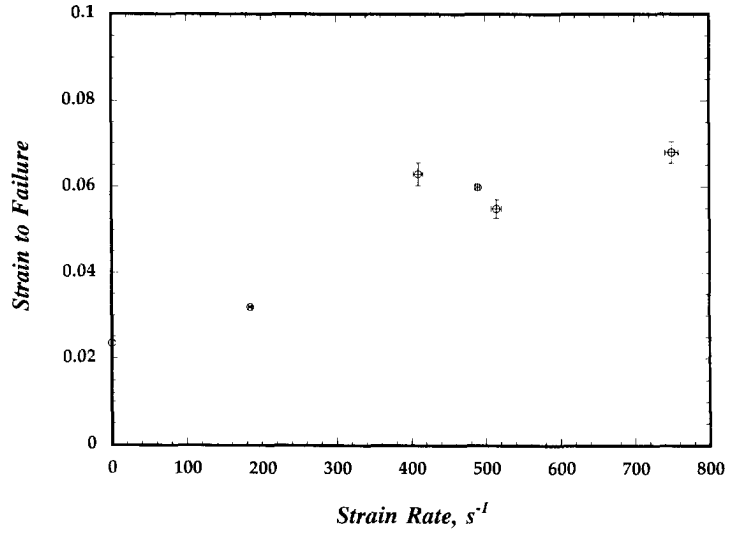

Fig. 8. The influence of the strain rate on the strain to failure of the composite. The quasistatic strain to failure is not accurately known since the extensometer was removed at 1.2% to prevent damage; the quasistatic elongation at failure was 3.5%.

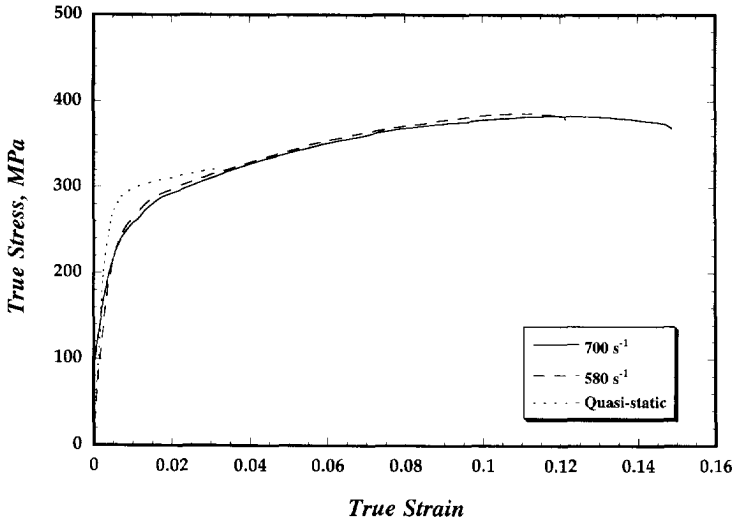

Fig. 9. Dynamic and quasistatic true stress–true strain curves for the monolithic alloy under tension. Note the much greater ductility of the monolithic alloy relative to that of the composite (Fig. 7).

alloy and the composite have very different strain hardening behaviors in dynamic tension. This represents further evidence of the development of internal damage in the composite in tension; no damage is expected in the compressive case.

The nature of the fractures developed during dynamic tension in the composite and the monolithic alloy can be inferred from Figs 10(a,b). The composite specimens show a macroscopically brittle fracture, with little or no necking, while the alloy specimens show macroscopically ductile fracture with necking and the formation of cup and cone fracture surfaces. Scanning electron micrographs of the fracture surface of the monolithic alloy and the composite are presented in Figs 11 and 12.

Figure 11(a) shows the fracture surface of the monolithic alloy and is an example of a classical ductile fracture, with a relatively homogeneous distribution of dimples (the result of void growth and coalescence) over the entire surface. The average dimple size is somewhat larger than 10 μm. When examined under higher magnifications, as in Fig. 11(b), a population of much smaller dimples (of the order of 1 μm in size) is observed, generally

connecting the larger dimples. These represent void sheet formation during the growth and coalescence of the voids to form the overall fracture surface.

The fracture surface of the composite (fractured in dynamic tension) is shown in Fig. 12(a). Even though the fracture was macroscopically brittle, the fracture surface itself is composed entirely of dimples resulting from void growth and coalescence. Thus the composite shows macroscopically brittle behavior but a microscopically ductile failure process. Figure 12(a) is a representative picture of the fracture surface for all the high strain rate tests; there is no change in the fracture process itself. A statistical measure based on four micrographs taken from different portions of the fracture surface of one specimen showed that more than 70% of the dimples in the fracture surface contained a particle. Since this is true of both the mating fracture surfaces it follows that particle fracture dominates the process rather than particle pullout. Further, the fact that the area fraction of particles visible on the fracture surface is substantially greater than the volume fraction of the particles in the composite itself indicates that the fracture surface passed preferentially through particle-rich areas rather than simply propagating transverse to the tensile axis. This would imply that the nucleation of the voids occurs preferentially near or at particles, which themselves fail in a brittle manner.

The existence of the dimples in Fig. 12(a) indicates a ductile failure in the matrix. Indeed, careful examination shows that some void sheeting occurs even in the composite, although the mechanism is less common than in the monolithic alloy. Note that the average dimple size in the composite is somewhat larger than for the monolithic alloy, as a result of the relatively large particle size. This is consistent with the hypothesis that void nucleation begins at the particles themselves. An examination of the fracture surface at greater magnification [Fig. 12(b)] shows some debonding has also occurred between the particle and the matrix. This process of debonding, beginning from a crack within the particle, is thought to nucleate the void itself around each particle. Occasionally particle pullout is also observed, as in Fig. 12(b), although the majority of the dimples contain fractured particles. Similar features were observed during the quasistatic fracture of alumina-reinforced 6061 composites by Liu and Lewandowski (1993).

The process of failure can be elucidated by examining the development of damage along the tensile axis as one moves away from the fracture surface. Figure 13 shows a scanning electron micrograph of a longitudinal section of a fractured composite specimen at a point quite close to the fracture surface. A number of microcracked alumina particles are observed, with the microcracks aligned normal to the tensile axis. The larger the particle, the higher the probability that it will contain microcracks, consistent with the work of Brechet *et al.* (1991) and others. There is little evidence in this micrograph for general particle–matrix interface failure or for void growth in the matrix alone. As one moves away from the fracture surface along the tensile axis, the density of the microcracks that can be observed falls sharply, suggesting that the failure process itself quickly localizes. There is no evidence of any damage at distances sufficiently far (a distance of approximately half the specimen diameter) from the fracture surface.

A plausible hypothesis for the development of the dynamic failure process may be developed on the basis of these observations as follows. The first phase in the development of the failure consists of the occurrence of microcracks in the alumina particles, with the larger particles cracking first. This would be consistent with the fact that microcracking is almost the only damage mode observed along the tensile axis away from the fracture surface, and with the ideas associated with the Weibull distribution, considering the relatively large size of the particles. The next phase in the failure process is hypothesized to consist of partial debonding at the particle–matrix interface, resulting in the nucleation of what is essentially a void within the matrix. The fact that debonding occurs is evident from the microscopic examination of the fracture surface, and the concept of particle cracking occurring before the nucleation and growth of the voids is consistent with the observation that most of the dimples on the fracture surface contain a fractured particle. This mode of void nucleation essentially results in relatively large voids, since the particles are 21 μm on average. In the final stage of the failure process, the voids grow and coalesce through ductile flow of the matrix, sometimes linking up through void sheets. This is of course evident from

examination of the fracture surface. The overall process described above is similar to that reported by Liu and Lewandowski (1993) during the quasistatic fracture of a similar material (with the matrix in different aging conditions).

The relatively localized nature of the damage within the composite specimens is also of some interest. A similar behavior was observed by Lloyd (1991) within a 6061 aluminum alloy reinforced with SiC particles; he concluded that this was a result of a smaller strain range prior to fracture for a matrix in the peak aged condition than in an underaged condition. Thus the contribution to the total strain from the localized region in which most of the damage develops can be substantial.

6. CONCLUSIONS

The dynamic failure of an alumina particle-reinforced 6061-T6 aluminum alloy composite has been studied using a tension Kolsky bar, and the process of fracture has been investigated using scanning electron microscopy. The failure of a 6061-T6 aluminum alloy was also studied for purposes of comparison. The composite was found to fail in a macroscopically brittle manner in tension, with a failure strain that increased with the nominal strain rate. The stress–strain curves of the composite in dynamic tension were found to show negligible hardening, whereas the dynamic compressive response of the same material showed substantial strain hardening. The differences in hardening rate between tension and compression were ascribed to the development of internal damage within the composite in the form of particle cracking. Examination of the fracture surface of the monolithic alloy after dynamic failure showed a ductile failure through void nucleation, growth and coalescence, with substantial void sheet formation. Examination of the fracture surface of the composite after dynamic failure showed microscopically ductile failure in the matrix following brittle cracking of the particles. The dynamic failure process is hypothesized to consist of: (a) cracking of the reinforcing particles; (b) partial debonding at the particle–matrix interface resulting in the nucleation of voids within the matrix; and (c) the growth and coalescence of voids in the matrix to form the final failure surface. This basic process is similar to that observed during the quasistatic fracture of such composites. The failure process itself quickly localizes within the specimen, so that only a small part of the specimen is affected by all of the damage processes of particle cracking, interface failure and void growth.

Acknowledgements—This work was supported by the U.S. Army Research Office under Award No. DAAL0391G0079 to K. T. Ramesh. The authors are pleased to acknowledge helpful discussions with G. Bao, K. J. Hemker and M. da Silva. This work is dedicated to the memory of Professor Jacques Duffy.

REFERENCES

Arsenault, R. J. and Taya, M. (1987). Thermal residual stress in metal matrix composite. *Acta Metall.* **35,** 651–659.

Arsenault, R. J. and Wu, S. B. (1987). The strength differential and Bauschinger effects in SiC/Al composites. *Mater. Sci. Engng* **96,** 77–88.

Bao, G. (1992). Damage due to fracture of brittle reinforcements in a ductile matrix. *Acta Metall. Mater.* **40,** 2547–2555.

Bao, G., Hutchinson, J. W. and McMeeking, R. M. (1991). Particle reinforcement of ductile matrices against plastic flow and creep. *Acta Metall. Mater.* **39,** 1871–1882.

Brechet, Y., Embury, J. D., Tao, S. and Luo, L. (1991). Damage initiation in metal matrix composite. *Acta Metall. Mater.* **39,** 1781–1786.

Cho, K., Lee, S., Chang, Y. W. and Duffy, J. (1991). Dynamic fracture behavior of SiC whisker-reinforced aluminum alloys. *Metall. Trans. A* **22A,** 367–375.

Christman, T., Needleman, A., Nutt, S. and Suresh, S. (1989a). On microstructural evolution and micromechanical modeling of deformation of a whisker-reinforced metal–matrix composite. *Mater. Sci. Engng A* **107,** 49–61.

Christman, T., Needleman, A. and Suresh, S. (1989b). An experimental and numerical study of deformation in metal–ceramic composites. *Acta Metall.* **37,** 3029–3050.

Clegg, W. J. (1988). A stress analysis of the tensile deformation of metal–matrix composites. *Acta Metall.* **36,** 2141–2149.

Clifton, R. J. and Klopp, R. W. (Editors) (1985). *Pressure-Shear Plate Impact Testing*, 9th Edn, pp. 230–239, Vol. 8. American Society of Metals Handbook, ASM International.

Davidson, D. L. (1991). Tensile deformation and fracture toughness of 2014+15 Vol. Pct. SiC particulate composite. *Metall. Trans. A* **22A,** 113–123.

Espinosa, H. D. and Clifton, R. J. (1991). Plate impact experiments for investigating inelastic deformation and damage of advanced materials. In *Experiments in the Micromechanics of Failure Resistant Materials* (Edited by K. S. Kim). *AMD-ASME* **130,** 37–56.

Evans, A. G., Hutchinson, J. W. and McMeeking, R. M. (1991). Stress–strain behavior of metal matrix composites with discontinuous reinforcements. *Scripta Metall. Mater.* **25,** 3–8.

Flom, Y. and Arsenault, R. J. (1989). Effect of particle size on fracture toughness of SiC/Al composite material. *Acta Metall.* **37,** 2413–2423.

Harding, J., Taya, M., Derby, B. and Pickend, S. (1987). *Proceedings of the ICCM-6/ECCM-2* (Edited by F. L. Matthews). pp. 2.224–2.233. Elsevier Applied Science.

Hunt, W. H., Jr, Brockenbrough, J. R. and Magnusen, P. E. (1991). An Al–Si–Mg composite model system: microstructural effects on deformation and damage evolution. *Scripta Metall. Mater.* **25,** 15–20.

Kamat, S. V., Hirth, J. P. and Mehrabian, R. (1989). Mechanical properties of particulate-reinforced aluminum–matrix composites. *Acta Metall.* **37,** 2395–2402.

Lewandowski, J. J., Liu, C. and Hunt, W. H. (1989). Effects of matrix microstructure and particle distribution on fracture of an aluminum metal matrix composite. *Mater. Sci. Engng A* **107,** 241–255.

Lewandowski, J. J., Liu, D. S. and Liu, C. (1991). Observations on the effects of particulate size and superposed pressure on deformation of metal matrix composites. *Scripta Metall.* **25,** 21–26.

Liu, D. S. and Lewandowski, J. J. (1993). The effects of superimposed hydrostatic pressure on deformation and fracture: Part II. Particulate-reinforced 6061 composites. *Metall. Trans. A* **24A,** 609–615.

Liu, D. S., Manoharan, M. and Lewandowski, J. J. (1989). Effects of microstructure on the behavior of an aluminum-alloy and an aluminum matrix composite tested under low levels of superimposed hydrostatic pressure. *Metall. Trans. A* **20,** 2409–2417.

Llorca, J., Needleman, A. and Suresh, S. (1991). An analysis of the effects of matrix void growth on deformation and ductility in metal–ceramic composites. *Acta Metall. Mater.* **39,** 2317–2335.

Lloyd, D. J. (1991). Aspects of fracture in particulate reinforced metal matrix composites. *Acta Metall. Mater.* **39,** 59–71.

Marchand, A., Duffy, J., Christman, T. A. and Suresh, S. (1988). An experimental study of the dynamic mechanical properties of an Al–SiCw composite. *Engin. Fracture Mech.* **30,** 295–315.

Mummery, P. and Derby, B. (1991). The influence of microstructure on the fracture-behavior of particulate metal matrix composites. *Mater. Sci. Engng A* **135,** 221–224.

Nair, S. V., Tien, J. K. and Bates, R. C. (1985). SiC reinforced aluminum metal–matrix composites, a review. *Int. Metall. Rev.* **30,** 275–290.

Papazian, J. M. and Adler, P. N. (1990). Tensile properties of short fiber-reinforced SiC/Al composites: Part I. Effects of matrix precipitates. *Metall. Trans. A* **21A,** 401–410.

Perng, C.-C., Hwang, J.-R. and Doong, J.-L. (1993). The effect of strain rate on the tensile properties of an Al_2O_3/6061-T6 aluminum metal–matrix composite at low temperatures. *Scripta Metall. Mater.* **29,** 311–316.

Rajendran, A. M., Bless, S. J. and Dawicke, D. S. (1986). Evaluation of Bodner–Partom model parameters at high strain rate. *J. Engng Mater. Tech.* **108,** 75–80.

Ramesh, K. T. (1994). On the localization of shearing deformations in tungsten heavy alloys. *Mech. Mater.* **17,** 165–173.

Ramesh, K. T. and Coates, R. S. (1992). Microstructural influences on the dynamic response of tungsten heavy alloys. *Metall. Trans. A* **23A,** 2625–2630.

Singh, P. M. and Lewandowski, J. J. (1993). Effects of heat treatment and reinforcement size on reinforcement fracture during tension testing of a SiCp discontinuously reinforced aluminum alloy. *Metall. Trans. A* **24A,** 2531–2543.

Staab, G. H. and Gilat, A. (1991). A direct-tension split Hopkinson bar for high strain-rate testing. *Exp. Mech.* **31,** 232–235.

Strangwood, M., Hippsley, C. A. and Lewandowski, J. J. (1991). Interfacial segregation in Al based metal matrix composites, pp. 97–108. TMS, Warrendale, Pennsylvania.

Taggart, D. G. and Bassani, J. L. (1991). Elastic–plastic behavior of particle reinforced composites—influence of residual stresses. *Mech. Mater.* **12,** 63–80.

Tvergaard, V. (1990). Analysis of tensile properties for a whisker reinforced metal–matrix composite. *Acta Metall. Mater.* **38,** 185–194.

Yadav, S., Chichili, D.R. and Ramesh, K. T. (1995). The mechanical response of a 6061-T6 Al/Al_2O_3 metal–matrix composite at high rates of deformation. *Acta Metall. Mater.* (in press).

Yang, J., Cady, C., Hu, M. S., Zok, F., Mehrabian, R. and Evans, A. G. (1990). Effects of damage on the flow strength and ductility of a ductile Al alloy reinforced with SiC particulates. *Acta Metall. Mater.* **38,** 2613–2619.

Yang, J., Pickard, S. M., Cady, C., Evans, A. G. and Mehrabian, R. (1991). The stress/strain behavior of aluminum matrix composites with discontinuous reinforcements. *Acta Metall. Mater.* **39,** 1863–1869.

Zhou, Z., Song, Z. J. and Xu, Y. K. (1991). Effect of microstructure on the mechanical properties of an Al alloy 6061 SiC particle composite. *Mater. Sci. Engng A* **1321,** 83–88.